CONTRAST MEDIA & MOLECULAR IMAGING

Received: 12 August 2014, Revised: 6 February 2015, Accepted: 13 February 2015, Published online in Wiley Online Library: 30 April 2015

(wileyonlinelibrary.com) DOI: 10.1002/cmmi.1639

Nanoparticle-stabilized microbubbles for multimodal imaging and drug delivery

Ýrr Mørch[a]*, Rune Hansen[b], Sigrid Berg[b], Andreas K. O. Åslund[c], Wilhelm R. Glomm[a,d], Siv Eggen[c], Ruth Schmid[a], Heidi Johnsen[a], Stephan Kubowicz[a], Sofie Snipstad[c], Einar Sulheim[c], Sjoerd Hak[c,e], Gurvinder Singh[d], Birgitte H. McDonagh[d], Hans Blom[f], Catharina de Lange Davies[c] and Per M. Stenstad[a]

Microbubbles (MBs) are routinely used as contrast agents for ultrasound imaging. The use of ultrasound in combination with MBs has also attracted attention as a method to enhance drug delivery. We have developed a technology platform incorporating multiple functionalities, including imaging and therapy in a single system consisting of MBs stabilized by polyethylene glycol (PEG)-coated polymeric nanoparticles (NPs). The NPs, containing lipophilic drugs and/or contrast agents, are composed of the widely used poly(butyl cyanoacrylate) (PBCA) polymer and prepared in a single step. MBs stabilized by these NPs are subsequently prepared by self-assembly of NPs at the MB air–liquid interface. Here we show that these MBs can act as contrast agents for conventional ultrasound imaging. Successful encapsulation of iron oxide NPs inside the PBCA NPs is demonstrated, potentially enabling the NP–MBs to be used as magnetic resonance imaging (MRI) and/or molecular ultrasound imaging contrast agents. By precise tuning of the applied ultrasound pulse, the MBs burst and the NPs constituting the shell are released. This could result in increased local deposit of NPs into target tissue, providing improved therapy and imaging contrast compared with freely distributed NPs. Copyright © 2015 John Wiley & Sons, Ltd.

Keywords: poly(butyl cyanoacrylate); nanoparticle; microbubble; targeted drug delivery; theranostics; focused ultrasound

1. INTRODUCTION

Nanoparticles (NPs) as carriers for cytotoxic drugs are of great interest in cancer therapy due to the enhanced permeability and retention effect (1). However, the uptake of NPs in tumors is often low and the distribution heterogeneous (2). In recent years, ultrasound has been shown to enhance the delivery of various NPs to tumors in small animals (3–5). Thus, ultrasound-mediated enhancement in delivery of NPs, which might be further enhanced in the presence of microbubbles (MBs), is clinically interesting. MBs might increase the heterogeneous vascular permeability by causing shear stress and jet streams, and the jet streams might also improve the penetration through the extracellular matrix. Ultrasound and MBs might also improve the delivery of non-encapsulated drugs, as recently demonstrated in a clinical study combining ultrasound and co-injection of gemcitabine and commercially available MBs to treat pancreatic cancer (6). In pre-clinical studies, the combination of ultrasound and MBs also facilitates a transient and local opening of the blood–brain barrier (7), thereby permitting various drugs to enter the brain and potentially treat central nervous system (CNS) disorders. As for all tissues, the exact mechanism by which ultrasound and MBs causes blood–brain barrier disruptions is not fully understood, but cavitation, i.e. volume oscillations of MBs in an ultrasound field, is obviously an important factor (8,9).

Poly(alkylcyanoacrylate) (PACA), first introduced to the medical field as surgical glue, has in recent years been extensively studied as a material for drug delivery vehicles (10,11). PACA NPs can easily be prepared by *in situ* polymerization of alkylcyanoacrylate monomers encapsulating a wide range of drugs with high loading capacity. As the monomers are hydrophobic, PACAs are especially suitable for encapsulating lipophilic drugs, thereby improving the delivery of poorly blood-soluble

* *Correspondence to: Ý. Mørch, SINTEF Materials and Chemistry, P.O. Box 4760 Sluppen, 7465 Trondheim, Norway. E-mail: yrr.morch@sintef.no*

a *Ý. Mørch, W. R. Glomm, R. Schmid, H. Johnsen, S. Kubowicz, P. M. Stenstad*
SINTEF Materials and Chemistry, P.O. Box 4760 Sluppen, 7465 Trondheim, Norway

b *R. Hansen, S. Berg*
SINTEF Technology and Society, P.O. Box 4760 Sluppen, 7465 Trondheim, Norway

c *A. K. O. Åslund, S. Eggen, S. Snipstad, E. Sulheim, S. Hak, C. Davies*
Department of Physics, Norwegian University of Science and Technology, 7491 Trondheim, Norway

d *W. R. Glomm, G. Singh, B. H. McDonagh*
Department of Chemical Engineering, Norwegian University of Science and Technology, 7491 Trondheim, Norway

e *S. Hak*
Department of Circulation and Medical Imaging, Norwegian University of Science and Technology, 7030 Trondheim, Norway

f *H. Blom*
Science for Life Laboratory, Box 1031, 17121 Solna, Sweden

drugs. The flexibility of the PACA nanoparticulate system allows for good control and design of end-use properties. The size and degradation rate can be regulated, and the surface functionalized (12), allowing for long circulation times and targeted delivery. A common approach for avoiding clearance by the immune system is coating the NPs with polyethylene glycol (PEG). Another important feature of the NPs is the possibility to incorporate imaging agents such as fluorescent dyes and magnetic resonance imaging (MRI) or positron emission tomography/single-photon emission computed tomography (PET/SPECT) contrast agents, achieving a combination of therapeutics and diagnostics, so called 'theranostics' (13,14).

In this paper, we present a novel multimodal, multifunctional imaging and drug delivery platform composed of air MBs stabilized by polymeric NPs of poly(butyl cyanoacrylate) (PBCA). The main limitations of NPs with added functionalities have so far been additional synthesis steps and high costs (15). In contrast to other NP–MB systems previously described (16–18), our technology platform is based on NPs developed and optimized using a *one-step synthesis*, whereby all functionalities can be introduced in a controlled and straightforward manner. This process includes customizing the NP surface by introducing PEG groups and incorporating drugs and contrast agents for various imaging modalities. The PEGylated NPs are subsequently used to stabilize MBs by self-assembly of the NPs onto the MB surface. The method is simple, cheap, requires no organic solvents and is feasible to scale up.

Clinically approved ultrasound contrast agents consist of a suspension of gaseous MBs stabilized by a shell of lipids or protein. Here we show that our MBs with shells made of PBCA NPs can act as contrast agents for ultrasound imaging of the microcirculation. By precise tuning of the applied ultrasound pulse, the MBs will burst and the NPs constituting the shell are released. We hypothesize that the particles, given momentum from the burst of the bubble, can move towards targets outside the blood circulation as illustrated in Fig. 1. Local deposit of drugs or contrast agents into target tissue may provide the possibility to further visualize, quantify, treat and monitor disease at different stages using multiple imaging modalities including MRI.

The aims of the present study are to (i) characterize NPs and MBs with respect to size, size distribution, concentration, surface functionalization and stability, (ii) demonstrate the ability to incorporate hydrophobic drugs and MRI contrast agents and (iii) demonstrate the ultrasound imaging capabilities of the MBs.

2. MATERIALS AND METHODS

2.1. Synthesis of NPs and MBs

Miniemulsion polymerization was used to prepare PEGylated NPs consisting of the polymer PBCA (19–21). Oil-in-water emulsions were prepared by emulsifying (Branson Digital Sonifier) a monomer phase, consisting of butyl-2-cyanoacrylate (BCA, kind gift from Henkel Loctite), co-stabilizer MIGLYOL®810 N (2 wt%, kind gift from Cremer) and the fluorescent dye Nile red (0.4 wt %, Sigma) in an acidic aqueous medium (0.1 M HCl) containing sodium dodecyl sulfate (SDS; 0.4 wt%, Merck) as surfactant. The emulsification was carried out on ice using 60% amplitude of the ultrasonic homogenizer (13 mm diameter transducer, Branson) for a total of 3 min with 30 s intervals and 10 s pauses between intervals. The initiation of the anionic polymerization was carried out by adding a solution of polyetheramine (JEFFAMINE® M-1000, 2 wt% at pH 6, kind gift from Huntsman Corporation) to the emulsion, resulting in PEGylated NPs. For non-PEGylated particles NaOH was used as initiator. Excess PEG and SDS were removed by dialysis against distilled water (six dialysate changes) using dialysis membranes of regenerated cellulose with molecular weight cut off at 12–14 000 Da.

Air MBs were stabilized by self-assembly of the NPs at the air–water interface. For this, bovine serum albumin (BSA, Sigma), pH 7.5, was added to a NP suspension to a final concentration of 1 wt% of BSA and 1 wt% of NPs. The solution was vigorously stirred using an ULTRA-TURRAX® (IKA Werke) for 2 min at 20 500 rpm, resulting in stable MBs, as shown in Fig. 2. The average MB diameter could be controlled by varying the stirring speed (8000–24000 rpm).

2.2. Synthesis of Fe@Fe_3O_4 (core@shell) particles

Fe@Fe_3O_4 (core@shell) particles (5 or 12 nm) were incorporated into the polymer matrix, allowing detection by MRI. A detailed description of the magnetic nanoparticle synthesis has been reported previously (22). In brief, a solution of octadecene containing didodecyldimethylammonium bromide was heated to 120 °C, and after degassing the temperature was raised to 180 °C, and iron pentacarbonyl ($Fe(CO)_5$, Sigma Aldrich) was injected. The color of the solution slowly turns black, indicating the formation of nuclei. For encapsulation of magnetic nanoparticles, dried magnetic particles were added to the monomer

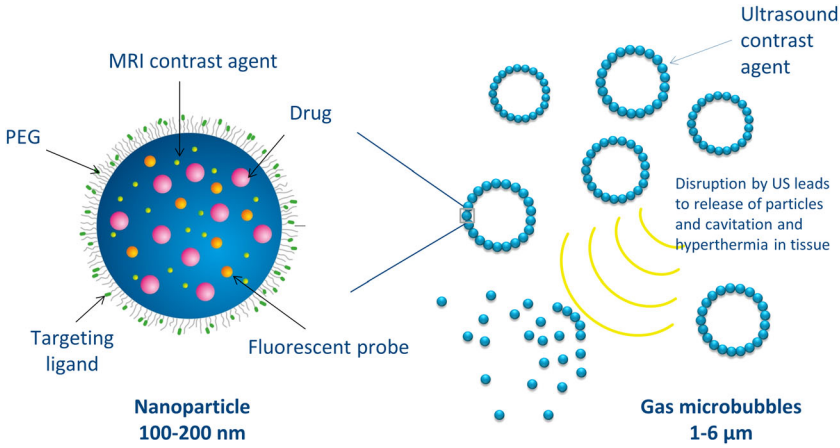

Figure 1. Schematic presentation of ultrasound-mediated delivery of the novel multifunctional and multimodal NP–MB platform. The generic technology platform opens up possibilities of incorporating ligands, drugs and imaging agents to meet the requirements of different applications.

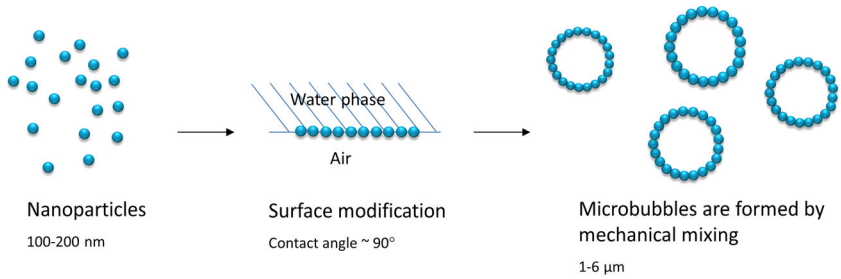

Figure 2. The principle of interfacial assembly of PBCA NPs at the MB surface. The desired hydrophobicity–hydrophilicity balance is obtained by mixing particles and proteins at pH 7.5.

solution at a concentration of ~7 mg mL^{-1} and dispersed in an ultrasonic bath for 3 h prior to emulsification. Energy dispersive X-ray spectroscopy (EDX) was performed to determine the presence of iron nanoparticles inside polymeric nanoparticles on a Hitachi S-5500 electron microscope operating at voltage 30 kV and current 20 µA.

The iron content in the particles was measured by inductively coupled plasma mass spectrometry (high-resolution ICP-MS, Element 2, Thermo Scientific). Samples were diluted 500-fold with deionized water and nitric acid added to 0.1 M.

Relaxivities were measured at room temperature on a 7 T Bruker scanner (BioSpec 70/20 AS, ParaVision 5.1, Bruker BioSpin MRI). Five sample dilution series (Fe concentration range 0.23–0.014 mM) were placed in a sample holder and T_1 and T_2 were measured with a so called rapid acquisition with relaxation enhancement (RARE) sequence (T_1 mapping, echo time (*TE*) of 10.7 ms, repetition time (*TR*) of 30, 50, 100, 200, 400, 800, 1500, 3000, 6000, 10 000, 15 000 ms, RARE factor of 2, FOV of 55 × 38 mm, matrix size (MTX) of 192 × 192, one slice of 2 mm, one average; T_2 mapping, *TE* of either 10, 20, 30, 40, 50, 60, 70, 80, or 20, 40, 60, 80, 100, 120, 140, 160 ms, *TR* of 15 000 ms, FOV of 55 × 38 mm, MTX of 76 × 84, one slice of 2 mm, one average). The obtained maps were analyzed with in-house built software in MATLAB. The relaxivity was obtained by plotting $1/T_1$ and $1/T_2$ as functions of Fe concentration. The slope of this plot represents the relaxivity with unit mM^{-1} s^{-1}.

2.3. Characterization of NPs and MBs

The hydrodynamic diameter of the NPs and their ζ-potential were determined by dynamic light scattering and laser Doppler velocimetry using a Zetasizer (Malvern, Nano ZS). The particle size and concentration were also determined using nanoparticle tracking analysis (NanoSight LM10-HS) and tunable resistive pulse sensing (qNano, Izon). qNano is a relatively novel system measuring the hydrodynamic size of each single particle passing through a pore. As the particle passes the pore the resistance of the electric circuit temporarily increases relative to the volume of the particle. For the qNano measurements, Nanopore NP150 and Nanopore NP1000 were used for detection of single NPs and NP aggregates, respectively. Particle morphology was determined by scanning transmission electron microscopy (STEM, Hitachi S-5500) by drying a diluted NP solution directly on a STEM stub followed by coating with 5 nm Au using a sputter coater. MBs imaged by STEM were embedded in poly(hydroxyethyl methacrylate) and microtomed prior to imaging.

The size distribution and concentration of MBs were determined using both a Coulter counter (Beckman Multisizer 3) and optical microscopy. The MBs were imaged using a bright field microscope with a 20×/0.25 objective, and after background subtraction the number of bubbles was counted and diameter determined using ImageJ's built-in Analyze Particles tool.

The fluorescently labeled NPs surrounding the MB were imaged by confocal laser scanning microscopy (CLSM) (LSM510, Zeiss), using a 40×/1.2 objective, and the incorporated dye Nile red was excited by a 488 nm laser. To improve the resolution to identify individual NPs, the particles were also imaged using a structural illumination microscope (super-resolution microscopy, SIM, Zeiss ELYRA PS) with a 63×/1.4 oil objective. The calibrated system gave a lateral (*xy*) resolution of about 100 nm.

2.4. Confirmation of PEGylation

PEGylation of particles was confirmed by ^{1}H-nuclear magnetic resonance (NMR) using a Bruker Avance DPX 400 MHz with autosampler. Prior to NMR, the dialyzed NPs were washed with distilled water and centrifuged three times before drying at 50 °C overnight. The samples were dissolved in acetone-D_6 and scanned for 32 scans. The spectra were processed in MestReNova 8.1 (Mestrelab Research) and the solvent residual peak at 2.05 ppm was used as reference. PEGylation was verified by locating the characteristic protons from PEG at 3.6 ppm. In order to calculate the concentration of PEG, the characteristic PEG peaks at 3.6 ppm and methylene group peaks of PBCA at 1.75 ppm and the peak of a triplet from MIGLYOL®810 N at 2.33 ppm were integrated. From the integrals, the number of protons corresponding to each integral, the dry weight of the material and the size and concentration of NPs, it was possible to calculate PEG nm^{-2}, assuming that all PEG molecules were situated at the interface. The effect of dialysis on the removal of excess PEG was also studied by measuring the total amount of PEG in the particle suspension prior to each dialysis step.

2.5. PBCA–protein interactions

Interaction between NPs and protein at pH 5.0 and pH 7.5 (at room temperature) was investigated using the Langmuir monolayer technique (KSV Langmuir Minitrough from KSV Instruments). A buffered NP solution was injected into a protein-containing sub-phase using the same NP and protein concentrations as for MB preparations, and the change in surface pressure was monitored over two steps. In the first step, the barriers were kept in constant position, and the change in surface pressure from interaction between the protein film and the injected NPs was measured over a period of 60 min. In the second step, the protein and protein–NP film were compressed at a constant rate of 5 mm min^{-1} in order to probe the film characteristics and strength via the 'injected' protocol (23,24).

2.6. Ultrasound imaging

Experimental procedures with animals were conducted in compliance with protocols approved by the Norwegian National Animal Research Authorities. Four female New Zealand White rabbits (Hsdlf:NZW, Harlan Laboratories, 10 weeks of age) were sedated with a solution of fentanyl 0.2 mg ml^{-1} and fluanisone 10 mg ml^{-1} (Hypnorm®, VetaPharma) at a dosage of 0.3 ml kg^{-1}. A 25G Venflon was inserted into the lateral ear vein, and anesthesia was induced by intravenous administration of midazolam 5 mg ml^{-1} (Midazolam B. Braun) at a dosage of 2 mg kg^{-1}. The hair on the ventral and lateral aspects of the rabbits' abdomens was removed using an electrical clipper. Bolus injections of various MB batches made with different stirring speeds and protein concentrations were given through the ear vein. Injection volumes varied from 0.05 ml to 1 ml, and number of bubbles per injection varied from 5×10^6 MBs to 3.6×10^8 MBs. All MBs were made at pH from 7.3 to 7.5, and with 1% (w/v) NPs. BSA concentration varied between 0.5 and 1% (w/v), and stirring speeds of 8000 rpm and 20 500 rpm were used. Ultrasound images were recorded using a GE Vivid E9 ultrasound scanner and a 9 L linear transducer (GE Vingmed Ultrasound). The images in contrast mode were obtained using a standard pulse inversion technique, transmitting at 3.6 MHz and receiving at 7.2 MHz using an mechanical index (MI) of 0.1–0.15 in the focal zone. When the ultrasound imaging was completed, the rabbits were euthanized by an intravenous administration of 5 ml of pentobarbital 100 mg ml^{-1}.

3. RESULTS

3.1. PEGylated PBCA NPs

Stable (i.e. non-aggregating) PEGylated PBCA nanoparticles (*z*-average 100–250 nm) were produced in one step using miniemulsion polymerization (Fig. 3 and Table 1). The nucleophilic amino group of the polyetheramine acts as initiator of the anionic polymerization of the BCA monomers and simultaneously grafts the PEG to the PBCA (25). The ingredients in the dispersed phase were mixed before the emulsification, resulting in an emulsion with an identical composition of encapsulated compounds and monomer in each droplet. The size distribution followed a Gaussian distribution with a polydispersity index (PDI) less than 0.2. The hydrophobic dye Nile red and Fe@Fe_3O_4 NPs were successfully encapsulated, allowing for optical and MR imaging of the particles (Fig. 4; see also Fig. 6 later). No magnetic particles were found outside PBCA NPs. Empty PBCA NPs could easily be separated from Fe@Fe_3O_4-containing NPs by magnet.

Table 1. Examples of PBCA NPs prepared by miniemulsion polymerization with and without PEG

NP diameter [nm]	PDI	ζ-potential [mV][a]	PEG chains/ [nm^2] [b]
153	0.1	−15	0.088
190	0.1	−35	0

[a]Measured in 10 mM phosphate buffer, pH 7.
[b]Measured by ^{1}H-NMR on dialyzed and washed particles.

The T_2 relaxivity of the obtained Fe@Fe_3O_4-containing NPs was 318 mM^{-1} s^{-1} (Fig. 4(c)), which is high and comparable to relaxivities reported in the literature for similar systems (26,27). This makes the NPs potentially well suited for use in T_2*-weighted MRI applications. The T_1 relaxivity was very low (1.6 mM^{-1} s^{-1}), which is also in line with values reported in the literature (26,28). Low T_1 relaxivity can be explained by the fact that bulk water has no access to the iron oxides residing in the hydrophobic NP core.

The concentration of PBCA NPs, measured as the dry weight, ranged between 3 and 14 wt%, corresponding to approximately 10^{12}–10^{14} NPs ml^{-1} in the final dialyzed particle suspension. The particle concentration was also measured directly using NanoSight and qNano, with the same results as above. The zeta potential decreased from −35 mV for non-PEGylated NPs to −15 mV for PEGylated NPs (Table 1).

PEGylation of the PBCA particles was confirmed by ^{1}H-NMR and the reduction in zeta potential (Fig. 5 and Table 1). The ^{1}H-NMR spectra revealed a characteristic PEG peak at 3.6 ppm for the PEGylated NPs. No such peak was seen in the spectrum for non-PEGylated NPs.

Excess PEG was removed by dialysis, and the particles were analyzed with ^{1}H-NMR after each step. The analysis revealed that most of the unbound PEG was removed during the first three dialysate exchanges, and after six dialysate exchanges only very low concentrations of free PEG were detected (data not shown). The bound PEG density was calculated after six dialysate exchanges and was found to be approximately 1 PEG per 11 nm^2, or about 6500 PEG chains per particle.

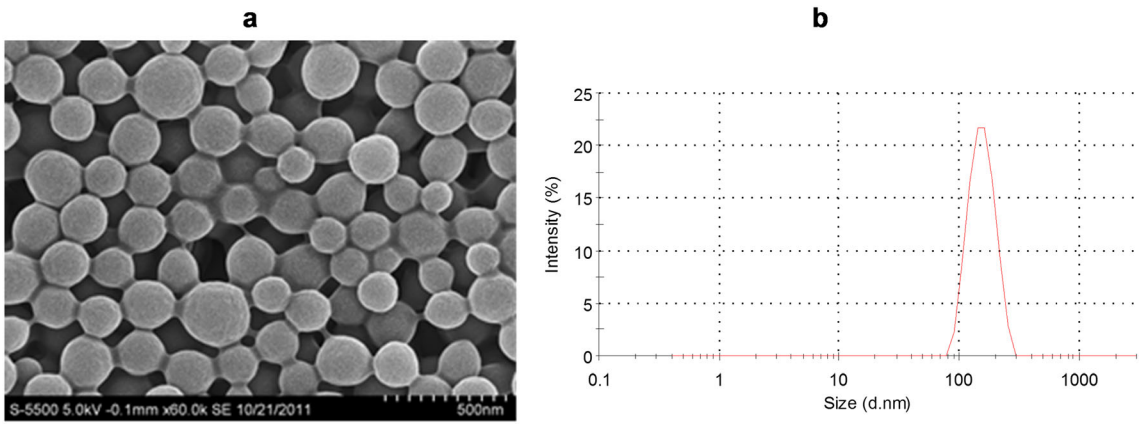

Figure 3. (a) STEM image of PEGylated PBCA NPs prepared in one step using the miniemulsion polymerization method. (b) Hydrodynamic diameter distribution of PEGylated PBCA particles measured by dynamic light scattering (Zetasizer).

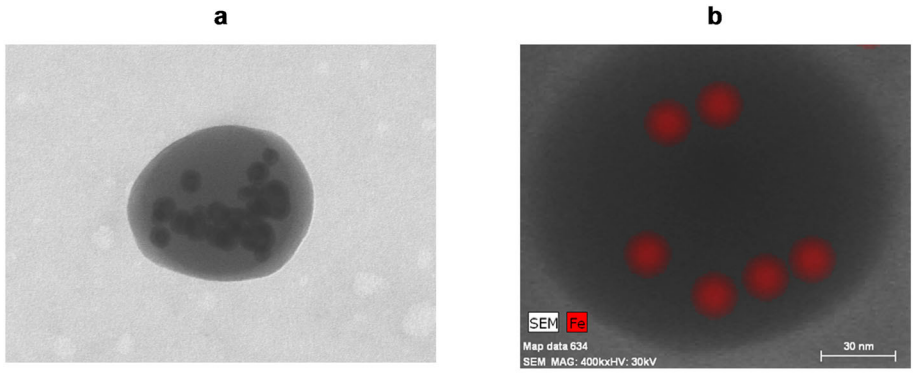

c

T1 relaxivity [$mM^{-1}s^{-1}$]	T2 relaxivity [$mM^{-1}s^{-1}$]
1.6	318

Figure 4. (a), (b) Bright-field TEM (a) and EDX area mapping (b) of PBCA NPs showing encapsulated Fe@Fe_3O_4 NPs (black and red spots in (a) and (b), respectively). (c) Relaxivity measurements of Fe@Fe_3O_4-containing PBCA NPs.

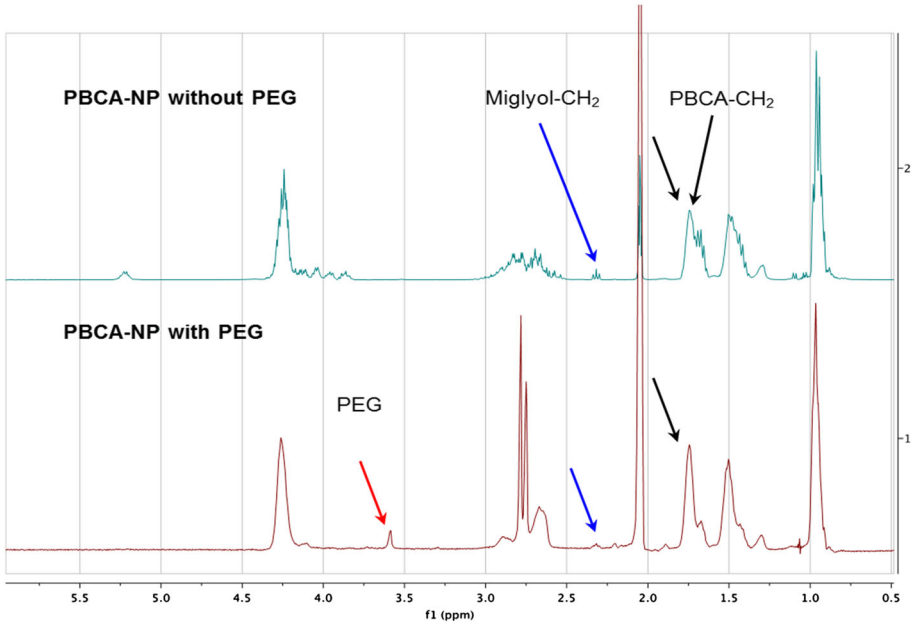

Figure 5. ^{1}H-NMR spectra for PBCA NPs without and with PEG.

3.2. NP-stabilized MBs

In the presence of BSA, PBCA NPs were able to stabilize gas-filled MBs. The particles self-assembled at the MB surface under vigorous mechanical stirring, producing NP-stabilized MBs. Moreover, MBs were remarkably stable, as shown in the light microscope images obtained immediately and 8 months after formation (Fig. 6(a), (b)). CLSM of the MBs (Fig. 6(c)) demonstrated that the NPs formed a shell around the MBs. In order to see the individual NPs on the MB surface, the MBs were also imaged using SIM, which provides a spatial resolution of 100 nm (Fig. 6(d)). STEM further revealed an outer layer of thickness corresponding to the diameter of one NP (Fig. 6(e)). Individual NPs could not be seen in this outer layer in the STEM images as they had melted into the embedding material. Using a mean diameter of 150 nm and 3 μm for NPs and MBs respectively, it was estimated that a single MB was covered with 1300–1500 NPs.

To investigate whether the MBs were decomposing and reforming over time, MBs were stabilized by non-fluorescent NPs before fluorescent NPs were added to the solution. CLSM imaging 24 h post-incubation with fluorescent NPs showed no fluorescence on the MB surface, indicating that the initially formed MBs were thermodynamically stable in solution (data not shown).

The shape of the MBs was rather heterogeneous (Figs 6 and 7). The size distribution of the MBs determined by light microscopy and image analysis showed that the diameter of MBs ranged from 1 to 6 μm (Fig. 7), with an average diameter of approximately 3 μm. Loaded NP–MBs (with iron oxide NPs or hydrophobic dye) were successfully produced within the same size and concentration range as compared with empty NP–MBs (Fig. 7(b)). The buckled

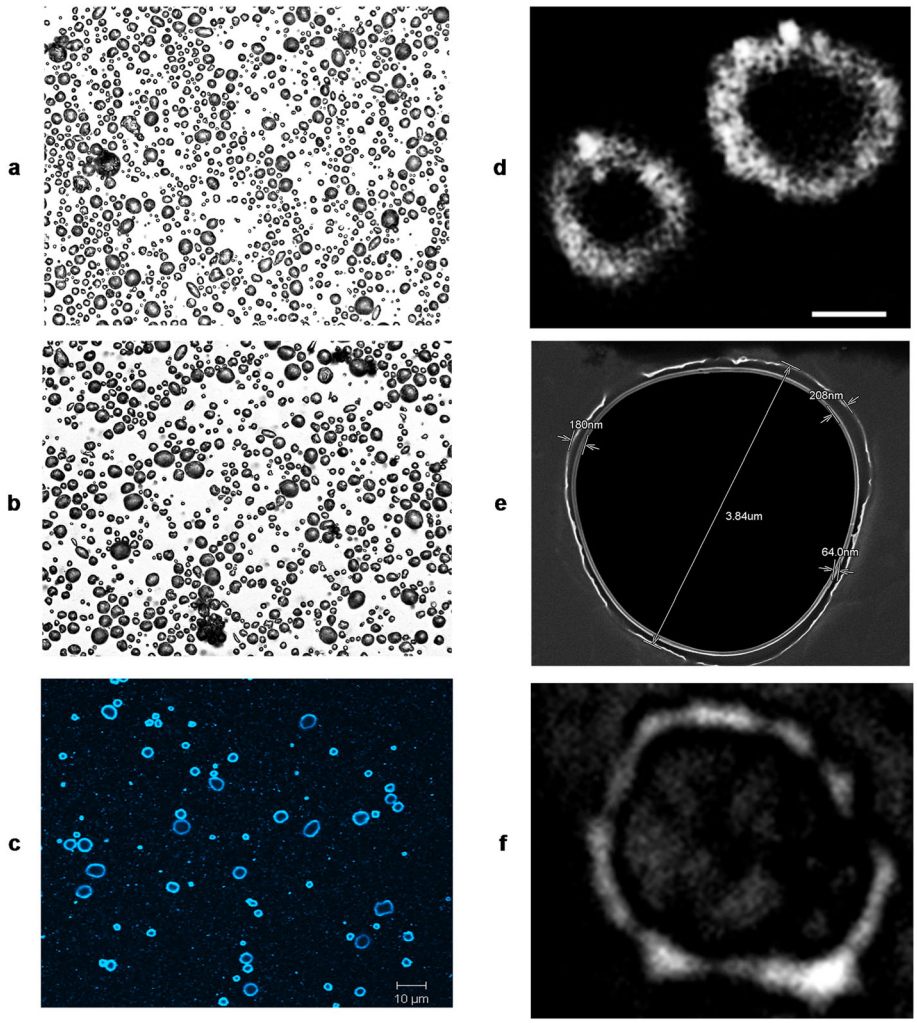

Figure 6. (a), (b) NP-stabilized MBs (1–6 µm) immediately (a) and 8 months (b) after preparation (stored in solution at 4 °C). (c) CLSM image of MBs demonstrating that the fluorescently labeled NPs form a shell around the MBs. (a)–(c) are taken with the same magnification. (d) NP-stabilized MBs imaged by SIM (scale bar 1 µm) demonstrated that Nile red-labeled NPs formed a layer of NPs around the MBs. (e), (f) In STEM images of MBs (e) individual NPs were not seen as they had melted into the embedding material, but were confirmed to be fluorescently labeled particles by CLSM imaging of the microtomed samples (f). The MB size in (f) is approximately 3 µm.

and non-spherical shape indicated a solid-like behavior of the MB shell.

For the MBs both the shell and size are critical factors for the acoustic properties. Thus the influence of varying different parameters during the production with respect to MB size and number was investigated (Fig. 8(a)–(c)). MB formation was vastly affected by the solution pH. Below pH 6 MBs could not be formed, whereas above pH 6 both MB size and number increased with increasing pH (Fig. 8(a)). Stable MBs could not be formed with either NPs or BSA alone; both components needed to be present. The optimum BSA concentration was found to be 1.0% (w/v); increasing the protein concentration further did not change the number of MBs (Fig. 8(b)). Moreover, the BSA concentration did not have any significant impact on the MB size. The size of the MBs could be controlled by the stirring speed of the ULTRA-TURRAX® (Fig. 8(c)). Increasing the stirring speed resulted in smaller bubbles and a higher concentration of MBs. Thus it is possible to tailor the size distribution of the MBs to desirable acoustic properties.

In order to further investigate how the solution pH affects the film-forming ability of protein and NPs and thus the ability to form stable bubbles, the Langmuir monolayer technique was used to study the film properties of BSA in the presence and absence of PBCA NPs (Fig. 9). Injecting BSA with PBCA NPs at pH 7.5 resulted in the strongest film-forming properties compared with any other combination investigated here. This means that stabilization of NPs with BSA is pH dependent, and that the most stable suspension is at physiological pH.

3.3. Ultrasound imaging of MBs in rabbits

Bolus injections of MBs were administered intravenously in rabbits, and images were recorded with the ultrasound transducer in a fixed position. The MB batches tested resulted in clear contrast enhancement in vessels and well-perfused organs such as kidney and liver. Ultrasound images showing the liver and gallbladder during an injection of 3.6×10^8 MBs are given in Fig. 10. As the MBs entered the arterial phase of the blood circulation the signal intensity in the ultrasound image in contrast mode increased. After only a few seconds the main arteries became bright due to backscattered signal from circulating bubbles (Fig. 10(c)) and after 17 s MBs contributed to high

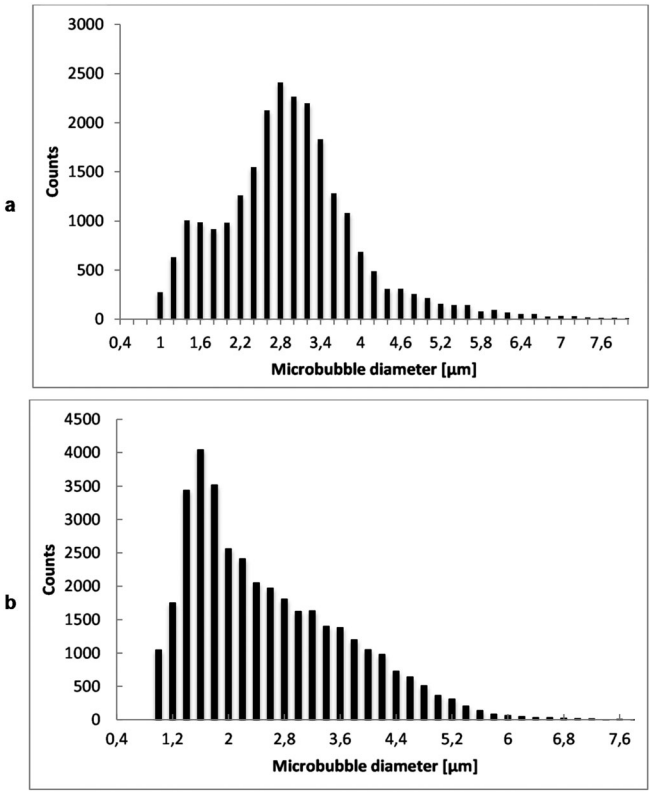

Figure 7. Representative histograms showing MB mean size distribution measured by light microscopy and image analysis of MBs stabilized by empty (a) and Fe@Fe_3O_4-loaded (b) NPs.

signals in both the arteries and the liver tissue (Fig. 10(d)). The gallbladder is however not perfused, and appeared dark throughout the imaging period.

Three regions of interest (ROIs) (diameter 1 mm) were selected in the image recorded during the administration of MBs (Fig. 10 (b)–(d)) and the signal intensity displayed as a function of time (Fig. 10(e)). The MBs first entered the artery (red line). The signal intensity increased by 20 dB between $t = 4$ s and $t = 9$ s, whereas the signal from the liver tissue (green line) increased gradually by 7–8 dB. The gall bladder had very low signal intensity throughout the scanning period (blue line). Breathing motion changed the ROI position within the imaged organ and caused fluctuations in the intensity curve presented in Fig. 10(e).

The animals were given several doses of MBs, and bubbles were detected even when the number of MBs was 70 times lower than in the given example. The intensity of the backscattered signal was however lower. No apparent adverse effects were observed in the animals. The ultrasound images in Fig. 10(b)–(d) were recorded at low pressures using an MI of 0.1. When the transmit pressures were increased, resulting in an MI of 0.25 or higher, the bubbles were destroyed and a strong backscattered burst was recorded. Ultrasound imaging of NP–MBs and the commercially available contrast agent SonoVue (Bracco Imaging) in tissue mimicking flow phantoms have shown that the pressure levels needed for bubble disruption are very similar. At a transmit frequency of 3.6 MHz bubbles burst at an MI of 0.2–0.25.

To confirm that single NPs and not aggregates were released as a result of bubble destruction, qNano was used to measure the number of aggregates in the MB solution before and after sonication at an MI high enough for bubble destruction. The

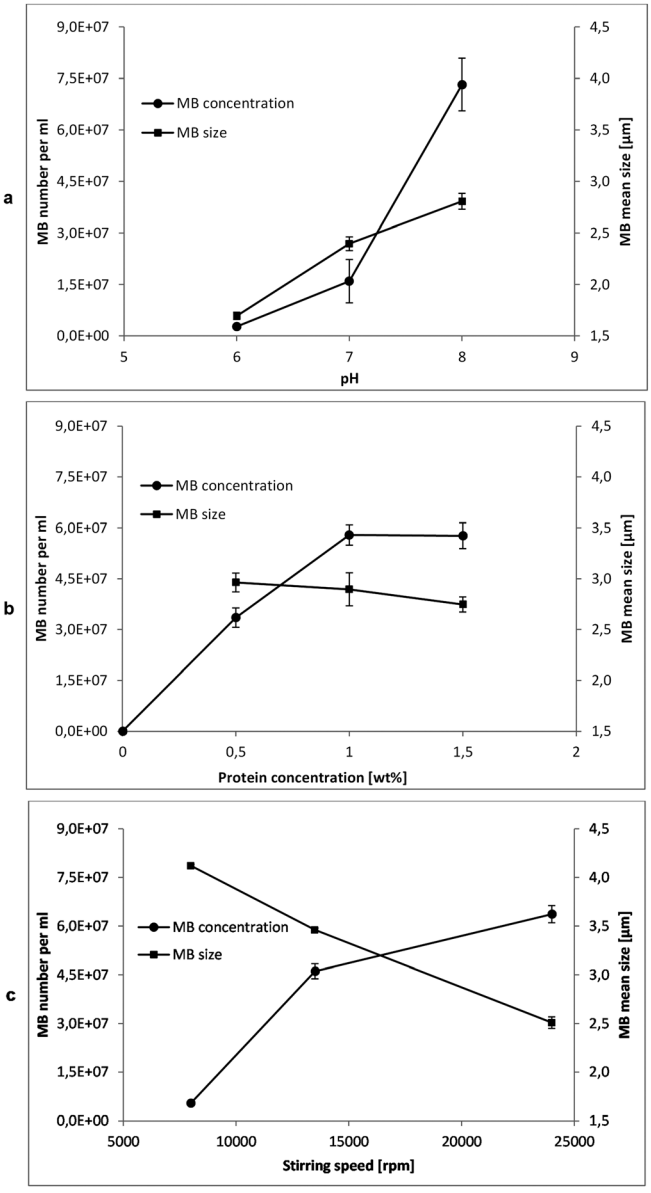

Figure 8. Mean MB concentration and mean MB diameter as a function of (a) pH, (b) albumin concentration and (c) stirring speed during preparation. Standard settings were NP concentration 1% (w/v), BSA concentration 1% (w/v), stirring speed 20 500 rpm and pH 7.5. The error bars represent standard deviation of mean MB size and distribution from three MB batches.

number of aggregates (size 600–1500 µm) did not change significantly, indicating that single NPs were released.

To see whether NPs could be destroyed by ultrasound, the NPs were exposed to high ultrasound power (MI up to 2.8 at 300 kHz). As expected due to the rigid structure of the polymeric particles, ultrasound did not affect the morphology of the NPs (data not shown).

4. DISCUSSION

4.1. PBCA NPs

Miniemulsion polymerization is a process that allows preparation of PEG-coated polymeric NPs by a one-step synthesis. Further, using PEG molecules with nucleophilic groups as the initiator

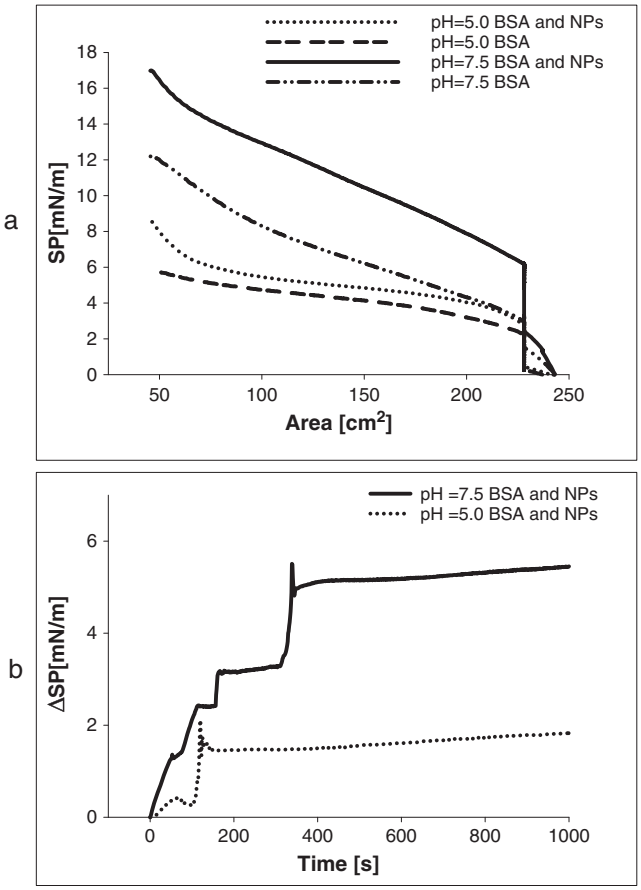

Figure 9. (a) Surface pressure–trough area compression isotherms of BSA and BSA + PBCA NPs at pH 5.0 and pH 7.5. (b) Change in surface pressure as a function of time upon injecting PBCA NPs underneath a BSA film at pH 5.0 and pH 7.5.

for the anionic polymerization of butyl cyanoacrylate monomers results in chemical bonding of PEG to PBCA polymer chains, which assures tightly bound PEG at the particle surface (25).

The negative surface charge on the PBCA particles likely emanates from partial hydroxylation of the ester groups of the PBCA chains, resulting in the formation of carboxylic acid groups. In addition, it cannot be ruled out that some negatively charged SDS is still associated with the particle surface even after extensive dialysis.

^{1}H-NMR showed that particles were PEGylated, but with a quite low surface coverage. During particle synthesis (polymerization), the stabilizer (SDS) is probably closely associated with the surface of the nanosized monomer emulsion droplets, leading to steric hindrance between the initiator (polyetheramine/PEG) and the droplet surface, thus limiting the overall PEGylation of the particles. Nevertheless, it was found that PEGylated particles had lower charge density compared with non-PEGylated NPs, indicating that PEG is shielding negative charges on the particle surface.

4.2. NP-stabilized MBs

Solid particles with intermediate hydrophobicity can adsorb strongly at the interface between immiscible fluids such as oil–water, enabling the formation of so-called Pickering emulsions (29), i.e. emulsions stabilized by solid particles of nano- or micrometer size. In the same manner, solid particles can be used to stabilize air–water interfaces. However, few materials inherently possess the sufficient balance of hydrophobicity and hydrophilicity essential for particle-stabilizing action. Only a scarce amount of literature exists on the topic of combining NP-stabilized MBs and drug delivery, likely due to the challenges associated with finding the right hydrophobic–hydrophilic balance (30). We have shown that PEGylated NPs of PBCA can be used to stabilize the air–water interface by self-assembly at the MB surface, resulting in very stable MBs.

The formation of NP-stabilized MBs in the present study required the addition of surface-active molecules – the protein BSA – and turbulent mixing. Particle adsorption alone is likely inhibited by a pronounced energy barrier due to electrostatic repulsion between particles, keeping them dispersed in the water phase. Alternatively, the stabilized particles are too hydrophilic, leading to preferential partitioning into the aqueous phase. This energy barrier can be overcome by applying high energy forces such as turbulent mixing and using a combination of particles and proteins giving an appropriate contact angle at the air–water surface (close to 90°) (31). Once particles are adsorbed at the interface of an air bubble, it is almost impossible to force them out of the interface, indicating a network formation at the interface. This was confirmed by adding fluorescent particles to an MB solution made of non-fluorescent particles, showing no exchange of NPs after bubble formation.

BSA is known to be a good surfactant, and the ability of albumin to stabilize air bubbles has previously been attributed to protein dimerization and hydrophobic interactions forming a thin protein film at the air–liquid interface (32). However, these bubbles have a very short lifetime and will dissolve spontaneously when infused intravenously. Here, we hypothesize that the PBCA NPs act as a branching unit, forming a network of higher-order protein multimers at the air–water interface. A shell of solid NPs around the MBs will eliminate the air–liquid surface tension and reduce the driving force of air out of the MBs.

The strong pH dependence on the formation of stable MBs is supported by the protein–NP interactions as studied using the Langmuir monolayer technique (Fig. 9). At pH 7.5, the interaction between PBCA NPs and BSA was significantly stronger and occurred much faster than at pH 5.0. Moreover, the BSA–PBCA NP film formed at the air–water surface at pH 7.5 was much stronger/more solid-like than found at pH 5, indicating that the PBCA NPs contribute more to the film properties at neutral pH. Considering that the pH conditions used here are approximately at (pH 5.0) and above (pH 7.5) the isoelectric point of BSA (pI ~ 4.8–5.0), with the interaction increasing with increasing protein charge, it is reasonable to assume that the interaction between BSA and PBCA NPs is largely electrostatic in nature. Adsorption of proteins onto negatively charged NPs above the isoelectric point of the protein has been well documented (33,34). Close to the pI the electrostatic interaction is weak, and the protein will likely be randomly oriented at the NP surface, whereas at pH 7.5 protein orientation is dictated by charge density matching between oppositely charged domains. BSA does not undergo any significant conformational changes in the pH range from pH 4 to pH 8 (35), which reinforces the hypothesis of the initial interaction between PBCA NPs and BSA being predominantly electrostatic in nature (36).

By exchanging BSA with human serum albumin and other proteins such as casein, stable NP–MBs could still be produced,

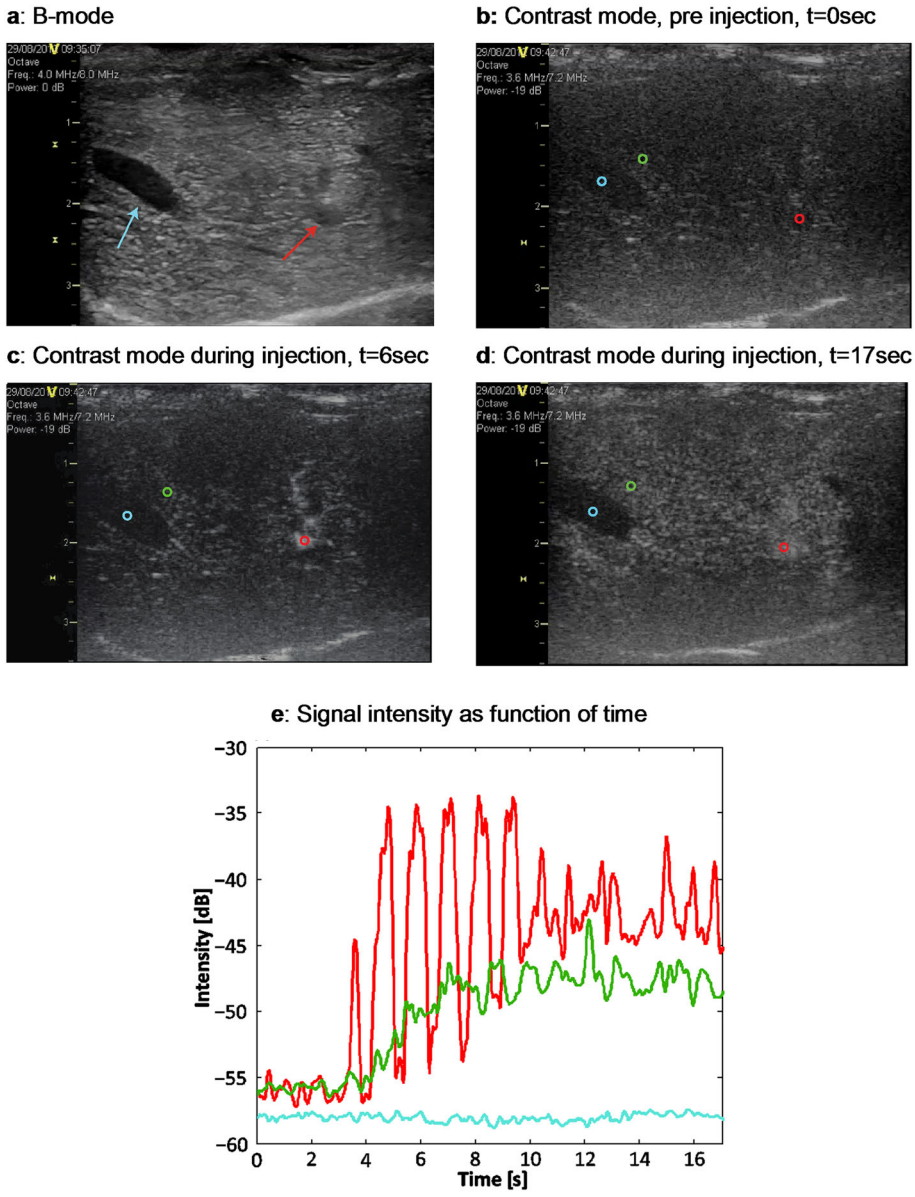

Figure 10. (a)–(d) Ultrasound images of a rabbit liver and gall bladder. (a) Ultrasound B-mode image showing the liver (grey area), the gall bladder (dark area indicated with blue arrow), some major blood vessels (also dark, marked with red arrow) and the diaphragm (bright line at the bottom of the image). (b)–(d) Images recorded in contrast mode during an injection of NP-stabilized MBs. Before the MBs entered the arterial circulation, most of the liver was dark (b). After a few seconds the main arteries became bright (c) and after 17 s MBs were contributing to high signal both in the arteries and the liver (d). (e) Signal intensity from circular regions of interest (ROIs) with diameter 1 mm in the gallbladder (blue), liver tissue (green) and large artery (red). The ROIs are displayed in (b)–(d). The bolus injection of the example shown was 3.6×10^8 MBs with a mean diameter of 3.1 μm.

although the concentration of protein had to be adjusted somewhat. NP–MBs stabilized by other proteins are currently being studied more extensively by our group.

The somewhat buckled and non-spherical MB shape suggests a solid-like shell behavior since equilibrium non-spherical shapes of ordinary bubbles are prohibited (37). Such behavior has recently been proposed to arise from the packing of adsorbed particles on the bubble interface. As the bubble area decreases (due to partly diffusion of air from the bubbles into the surrounding solution), excess particles cannot be released as they are irreversibly adsorbed, causing a wrinkled surface (37–39).

4.3. Ultrasound imaging of NP-stabilized MBs

Contrast-enhanced ultrasound imaging of the novel MBs in rabbits showed that they can be imaged by standard contrast agent imaging techniques implemented on clinical scanners, demonstrating that they are clinically interesting as ultrasound contrast agents. The MBs were injected intravenously, passed the lungs and entered the arterial side of the circulation system. As they circulated in well-perfused organs such as liver and kidney, the MBs provided a backscatter signal that was comparable to commercially available MBs such as SonoVue, and the NP–MBs could be destroyed with an MI in the range of 0.2–0.25 at

3.6 MHz. In small vessels, even single bubbles were detected. Multiple boluses of MBs could be injected without any acute adverse effects. However, since the rabbits were euthanized a few hours after injection of MBs, conclusions regarding long-term effects and toxicity cannot be drawn.

In vivo, MB circulation time can vary considerably. Hence, these MBs must be tested more thoroughly and systematically with regard to circulation time, and compared with commercially available MBs. This is being done in a follow-up study. MBs containing more hydrophobic gases such as perfluorocarbons are currently being explored in our laboratory in order to increase circulation time.

4.4. Clinical application of the NP–MBs

PBCA NPs have previously been used to stabilize air MBs to be used as an ultrasound contrast agent (40). However, to the best of our knowledge, a single NP–MB formulation incorporating multiple functionalities such as described here has not been reported previously by other groups. The unique feature of this NP–MB platform is the possibility for incorporating high payloads of drugs or other therapeutic agents as well as contrast agents for imaging. Using NPs to form the shell surrounding the MB might allow a higher payload of drugs compared with incorporating the drug into a solid polymeric shell layer as reported by others (41). In addition, since a surplus of NPs is used during MB production, free drug-loaded PEGylated NPs will be injected together with the NP–MBs, thus allowing for a high concentration of injected drug.

Integrating NPs and MBs into one single unit is found to be much more efficient in ultrasound-enhanced tumor uptake as compared with co-injection of NPs and MBs (17). This is probably caused by a higher concentration of NPs locally in the region of sonication where the MBs are destroyed. On the other hand, when NPs and MBs are co-injected intravenously the NPs are diluted in the bloodstream.

In accordance with this, we have recently demonstrated that focused ultrasound improved the distribution of our NPs in prostate xenografts growing in athymic mice (3), and the improved distribution of NPs was due to both enhanced extravasation across the capillary wall and improved penetration through the extracellular matrix.

The novel NP–MBs also provide possibilities for image-guided delivery of NPs using both contrast-enhanced ultrasound imaging and MRI (13,42), and the use of MRI to trace the NPs in various tissues. In addition, the NPs can be further targeted to specific biomarkers, allowing for active targeting and hence higher NP/drug accumulation at the disease site. Targeted MBs are currently being studied in our laboratories.

5. CONCLUSIONS

A combined nano/micro-imaging and drug delivery system was produced in a single formulation without the need of organic solvents. The PEG covalently attached on the particle surface allows for good colloidal stability and possibly increased blood circulation time. We have shown that this novel technology platform could potentially be used for simultaneous diagnostics and enhanced therapeutic effect. The flexibility of the system allows for tailoring to meet the requirements for imaging and treatment of various diseases including cancer, inflammation, CNS and cardiovascular diseases. The method is simple, cheap and easily scaled up, and should hence have potential for future theranostic applications.

Acknowledgements

The authors wish to thank Yngve Hansen MSc for assistance with microbubble characterization (Coulter counter) and Dr Annemieke van Wamel for kindly reading the manuscript. Henkel Loctite, Huntsman and Cremer are thanked for providing cyanoacrylate, JEFFAMINE® M-1000 and MIGLYOL® 810 N, respectively. The research was funded by The Research Council of Norway (project 220005), the Strategic Area of Medical Technology at NTNU, the Central Norway Health Authorities and the Norwegian Cancer Society. The Research Council of Norway is further acknowledged for the support to the Norwegian Micro- and Nano-Fabrication Facility, NorFab (197411/V30).

REFERENCES

1. Maeda H, Wu J, Sawa T, Matsumura Y, Hori K. Tumor vascular permeability and the EPR effect in macromolecular therapeutics: a review. J Control Release 2000; 65: 271–284.
2. Davies CdeL, Lundstrom LM, Frengen J, Eikenes L, Bruland OS, Kaahus O, Hjelstuen MHB, Brekken C. Radiation improves the distribution and uptake of liposomal doxorubicin (Caelyx) in human osteosarcoma xenografts. Cancer Res 2004; 64: 547–553.
3. Eggen S, Fagerland SM, Mørch Ý, Hansen R, Søvik K, Berg S, Furu H, Bøhn AD, Lilledahl MB, Angelsen A, Angelsen B, Davies CdeL. Ultrasound-enhanced drug delivery in prostate cancer xenografts by nanoparticles stabilizing microbubbles. J Control Release 2014; 187: 39–49.
4. Eggen S, Afadzi M, Nilssen EA, Haugstad SB, Angelsen B, Davies CdeL. Ultrasound improves the uptake and distribution of liposomal Doxorubicin in prostate cancer xenografts. Ultrasound Med Biol 2013; 39: 1255–1266.
5. Frenkel V. Ultrasound mediated delivery of drugs and genes to solid tumors. Adv Drug Deliv Rev 2008; 60: 1193–1208.
6. Kotopoulis S, Dimcevski G, Gilja OH, Hoem D, Postema M. Treatment of human pancreatic cancer using combined ultrasound, microbubbles, and gemcitabine: a clinical case study. Med Phys 2013; 40: 072902.
7. Burgess A, Hynynen K. Noninvasive and targeted drug delivery to the brain using focused ultrasound. ACS Chem Neurosci 2013; 4: 519–526.
8. Frenkel V. Ultrasound mediated delivery of drugs and genes to solid tumors. Adv Drug Deliv Rev 2008; 60: 1193–1208.
9. Humphrey VF. Ultrasound and matter – physical interactions. Prog Biophys Mol Biol 2007; 93: 195–211.
10. Nicolas J, Couvreur P. Synthesis of poly(alkyl cyanoacrylate)-based colloidal nanomedicines. Wiley Interdiscip Rev Nanomed Nanobiotechnol 2009; 1: 111–127.
11. Vauthier C, Dubernet C, Fattal E, Pinto-Alphandary H, Couvreur P. Poly(alkylcyanoacrylates) as biodegradable materials for biomedical applications. Adv Drug Deliv Rev 2003; 55: 519–548.
12. Vauthier C, Bouchemal K. Methods for the preparation and manufacture of polymeric nanoparticles. Pharm Res 2009; 26: 1025–1058.
13. Liu Z, Lammers T, Ehling J, Fokong S, Bornemann J, Kiessling F, Gaetjens J. Iron oxide nanoparticle-containing microbubble composites as contrast agents for MR and ultrasound dual-modality imaging. Biomaterials 2011; 32: 6155–6163.
14. Kiessling F, Fokong S, Bzyl J, Lederle W, Palmowski M, Lammers T. Recent advances in molecular, multimodal and theranostic ultrasound imaging. Adv Drug Deliv Rev 2014; 72: 15–27.
15. Cheng ZL, Al Zaki A, Hui JZ, Muzykantov VR, Tsourkas A. Multifunctional nanoparticles: cost versus benefit of adding targeting and imaging capabilities. Science 2012; 338: 903–910.
16. Lentacker I, Wang N, Vandenbroucke RE, Demeester J, De Smedt SC, Sander NN. Ultrasound exposure of lipoplex loaded microbubbles facilitates direct cytoplasmic entry of the lipoplexes. Mol Pharm 2009; 6: 457–467.
17. Burke CW, Alexander E, Timbie K, Kilbanov AL, Price RJ. Ultrasound-activated agents comprised of 5FU-bearing nanoparticles bonded

to microbubbles inhibit solid tumor growth and improve survival. Mol Ther 2014; 22: 321–328.
18. Park JI, Jagadeesan D, Williams R, Oakden W, Chung SY, Stanisz GJ, Kumacheva E. Microbubbles loaded with nanoparticles: a route to multiple imaging modalities. ACS Nano 2010; 4: 6579–6586.
19. Landfester K. Synthesis of colloidal particles in miniemulsions. Annu Rev Mater Res 2006; 36: 231–279.
20. Hansali F, Poisson G, Wu M, Bendedouch D, Marie E. Miniemulsion polymerizations of n-butyl cyanoacrylate via two routes: towards a control of particle degradation. Colloids Surf B Biointerfaces 2011; 88: 332–338.
21. Zhang Y, Zhu S, Yin L, Qian F, Tang C, Yin C. Preparation, characterization and biocompatibility of poly(ethylene glycol)-poly(n-butyl cyanoacrylate) nanocapsules with oil core via miniemulsion polymerization. Eur Polym J 2008; 44: 1654–1661.
22. Singh G, Kumar PA, Lundgren C, Helvoort ATJ, Mathieu R, Wahlström E, Glomm WR. Tunability in crystallinity and magnetic properties of core–shell Fe nanoparticles. Part Part Syst Char 2014; 31(10): 1054–1059.
23. Glomm WR, Volden S, Halskau O, Ese MHG. Same system – different results: the importance of protein. introduction protocols in Langmuir-monolayer studies of lipid–protein interactions. Anal Chem 2009; 81: 3042–3050.
24. Lystvet SM, Volden S, Yasuda M, Halskau O, Glomm WR. Emergent membrane-affecting properties of BSA–gold nanoparticle constructs. Nanoscale 2011; 3: 1788–1797.
25. Peracchia MT, Vauthier C, Popa M, Puisieux F, Couvreur P. Investigation of the formation of sterically stabilized poly(ethylene glycol isobutyl cyanoacrylate) nanoparticles by chemical grafting of polyethylene glycol during the polymerization of isobutyl cyanoacrylate. STP Pharma Sci 1997; 7: 513–520.
26. Ai H, Flask C, Weinberg B, Shuai X, Pagel MD, Farrell D, Duerk J, Gao JM. Magnetite-loaded polymeric micelles as ultrasensitive magnetic-resonance probes. Adv Mater 2005; 17: 1949–1952.
27. Xie XA, Zhang CF. Controllable assembly of hydrophobic superparamagnetic iron oxide nanoparticle with mPEG–PLA copolymer and its effect on MR transverse relaxation rate. J Nanomater 2011; 2011(2011): Article ID 152524. http://dx.doi.org/10.1155/2011/152524.
28. Jarzyna PA, Skajaa T, Gianella A, Cormode DP, Samber DD, Dickson SD, Chen W, Griffioen AW, Fayad ZA, Mulder WJM. Iron oxide core oil-in-water emulsions as a multifunctional nanoparticle platform for tumor targeting and imaging. Biomaterials 2009; 30: 6947–6954.
29. Pickering SU. Emulsions. J Chem Soc Trans 1907; 91: 2001–2021.
30. Du ZP, Bilbao-Montoya MP, Binks BP, Dickinson E, Ettelaie R, Murray BS. Outstanding stability of particle-stabilized bubbles. Langmuir 2003; 19: 3106–3108.
31. Stocco A, Rio E, Binks BP, Langevin D. Aqueous foams stabilized solely by particles. Soft Matter 2011; 7: 1260–1267.
32. Cavalieri F, Zhou M, Tortora M, Lucilla B, Ashokkumar M. Methods of preparation of multifunctional microbubbles and their in vitro/in vivo assessment of stability, functional and structural properties. Curr Pharm Des 2012; 18: 2135–2151.
33. Brewer SH, Glomm WR, Johnson MC, Knag MK, Franzen S. Probing BSA binding to citrate-coated gold nanoparticles and surfaces. Langmuir 2005; 21: 9303–9307.
34. Glomm WR, Halskau O, Hanneseth AMD, Volden S. Adsorption behavior of acidic and basic proteins onto citrate-coated Au surfaces correlated to their native fold, stability, and pI. J Phys Chem B 2007; 111: 14329–14345.
35. Carter DC, Ho JX. Structure of serum-albumin. Adv Protein Chem 1994; 45: 153–203.
36. Rezwan K, Meier LP, Rezwan M, Voros J, Textor M, Gauckler LJ. Bovine serum albumin adsorption onto colloidal Al_2O_3 particles: a new model based on zeta potential and UV–vis measurements. Langmuir 2004; 20: 10055–10061.
37. Subramaniam AB, Mejean C, Abkarian M, Stone HA. Microstructure, morphology, and lifetime of armored bubbles exposed to surfactants. Langmuir 2006; 22: 5986–5990.
38. Binks BP, Horozov TS. Aqueous foams stabilized solely by silica nanoparticles. Angew Chem Int Edn 2005; 44: 3722–3725.
39. Dickinson E, Ettelaie R, Kostakis T, Murray BS. Factors controlling the formation and stability of air bubbles stabilized by partially hydrophobic silica nanoparticles. Langmuir 2004; 20: 8517–8525.
40. Schmidt W, Roessling G. Novel manufacturing process of hollow polymer microspheres. Chem Eng Sci 2006; 61: 4973–4981.
41. Fokong S, Theek B, Wu ZJ, Koczera P, Appold L, Jorge S, Resch-Genger U, van Zandvoort M, Storm G, Kiessling F, Lammers T. Image-guided, targeted and triggered drug delivery to tumors using polymer-based microbubbles. J Control Release 2012; 163: 75–81.
42. Lammers T, Koczera P, Fokong S, Gremse F, Ehling J, Vogt M, Pich A, Storm G, Zandvoort M, Kiessling F. Theranostic USPIO-loaded microbubbles for mediating and monitoring blood–brain barrier permeation. Adv Funct Mater 2014. doi:10.1002/adfm.201401199.